




Field control of symmetry-broken and quantum disordered phases in frustrated moiré bilayers with population imbalance

Lorenzo Del Re ¹ and Laura Classen ^{1,2}

¹Max Planck Institute for Solid State Research, 70569 Stuttgart, Germany

²Department of Physics, Technical University of Munich, 85749 Garching, Germany

 (Received 7 November 2023; accepted 27 March 2024; published 22 April 2024)

We determine the ground states and excitation spectra of the paradigmatic four-flavor Heisenberg model with nearest- and next-nearest-neighbor exchange couplings on the triangular lattice in a field controlling the population imbalance of flavor pairs. Such a system arises in the strongly correlated limit of moiré bilayers of transition metal dichalcogenides in an electric displacement field or in-plane magnetic field, and can be simulated via ultracold alkaline-earth atoms. We argue that the field tunes between effective SU(4) and SU(2) symmetries in the balanced and fully polarized limits and employ a combination of mean-field calculations, flavor-wave theory, and exact diagonalization to analyze the intermediate, imbalanced regime. We find different symmetry-broken phases with simultaneous spin and excitonic order depending on the field and next-nearest-neighbor coupling. Furthermore, we demonstrate that there is a strongly fluctuating regime without long-range order that connects candidate spin liquids of the SU(2) and SU(4) limit. The strong fluctuations are facilitated by an extensive classical degeneracy of the model, and we argue that they are also responsible for a strong polarizability at 1/3 polarization that survives from the mean-field level to the exact spectrum.

DOI: [10.1103/PhysRevResearch.6.023082](https://doi.org/10.1103/PhysRevResearch.6.023082)

I. INTRODUCTION

Strong correlations and frustration in quantum systems constitute a promising combination in the quest for useful phases of matter. They have a high potential for the realization of unconventional spin orders with functional magnetic properties [1], as well as sought-after spin-liquid states with high entanglement and fractionalized excitations [2–4]. These phases are facilitated through a large degeneracy of the (classical) ground state (GS), which is why quantum spin models with various sources of degeneracy are intensely studied. For example, these include frustrated lattice geometries [5–11], higher SU(N) symmetries [12–23], or competing nearest- and next-to-nearest-neighbor interactions [24–37]. For their controlled design and manipulation, tunable [38–40] platforms are generally desirable, and even more so due to the fragile nature of quantum spin liquids.

The quantum simulation of strongly correlated fermions is established in ultracold atoms, and it was demonstrated that alkaline-earth atoms in optical lattices realize strongly correlated systems with a tunable number of flavors N and SU(N)-symmetric interactions [41–50]. Moiré transition metal dichalcogenides (TMDs) offer recent solid-state alternatives for the controlled study of strongly correlated electron systems, including triangular-lattice Hubbard models [51–68].

In particular, it is possible to form an SU(4) pseudospin out of layer and real spin degrees of freedom in twisted AB-stacked bilayers or three-layer hetero-structures with insulating middle layer [69]. In an experimental realization with WSe₂ competing electronic states with correlated insulators at integer fillings were reported [70]. An important tuning parameter in these experiments is given by a perpendicular electric field which controls the layer polarization. For integer layer populations, Mott insulators are formed at strong coupling, while at imbalanced layer populations, interlayer excitonic insulators (EIs) can emerge [70,71]. The Zeeman effect of an in-plane magnetic field and a population imbalance in cold-atom experiments acts analogously to such a polarizing field. All these fields detune the population of pairs of flavors against each other. Hence, they can be used to interpolate between effective SU(4) and SU(2) symmetric models from balanced to full polarization. This is particularly interesting for filling factors $n = 1$ or $n = 3$, where the SU(2) limit corresponds to the half-filled Hubbard model (as opposed to a band insulator for $n = 2$). Theoretically, however, the effect of layer or population imbalance is not well studied.

In this paper, we investigate population-imbalanced AB-stacked TMD bilayers and ultracold fermionic alkaline-earth atoms via the SU(4) symmetric triangular-lattice Heisenberg model in a field. We map out the phase diagram as a function of the imbalance P_z and next-to-nearest-neighbor coupling J' , employing flavor-wave theory and exact diagonalization. In previous studies of the SU(2) symmetric case, a quantum spin liquid (of debated nature) was found between a 120° and a stripe magnetic phase when J' is increased [27,28,30,34,35]. In the SU(4) limit, there is evidence for a transition from a quantum liquid to four-sublattice magnetic order upon

Published by the American Physical Society under the terms of the [Creative Commons Attribution 4.0 International license](https://creativecommons.org/licenses/by/4.0/). Further distribution of this work must maintain attribution to the author(s) and the published article's title, journal citation, and DOI. Open access publication funded by Max Planck Society.

increasing J' [19,22,69,72–74]. We show that one can tune between these two limits via an external field and determine the different GSs and their excitations in between. We find that the SU(2) 120° antiferromagnet (AFM) develops ferromagnetic (FM) “dopants” in the minority layer and simultaneous tripartite interlayer excitonic order when the field depopulates the half-filled majority layer. For larger J' , we obtain an evolution from the magnetic stripe order of the SU(2) limit into a four-sublattice state of the SU(4) limit with intermediate AFM and excitonic stripes. Furthermore, we demonstrate that a large part of the phase diagram is occupied by a strongly fluctuating phase (SFP) in which quantum fluctuations prevent any long-range order, and we argue that the SFP continuously connects the candidate spin liquids of the SU(2) and SU(4) limits.

II. THE MODEL

We depart from the triangular-lattice Hubbard model with four flavors per site $\alpha = \{|1\rangle, |2\rangle, |3\rangle, |4\rangle\}$. For concreteness, we identify these flavors with spin \uparrow, \downarrow and layer (top, bottom) degrees of freedom in moiré TMDs [69], i.e., $|1\rangle = |\uparrow t\rangle$, $|2\rangle = |\downarrow t\rangle$, $|3\rangle = |\uparrow b\rangle$, $|4\rangle = |\downarrow b\rangle$. In the strong coupling limit and at fillings $n = 1, 3$ electron(s) per site, the Hubbard Hamiltonian is well captured by the Heisenberg model [75]

$$H = \sum_{ij} J_{ij} S_{\beta}^{\alpha}(i) S_{\alpha}^{\beta}(j) + \delta \sum_i \hat{P}_i^z, \quad (1)$$

where $S_{\beta}^{\alpha} = |\alpha\rangle\langle\beta|$ and we consider nearest-neighbor (NN) and next-nearest-neighbor (NNN) superexchange processes J_{ij} of intensity J and J' , respectively. In addition, we add the layer polarization $\hat{P}^z = |1\rangle\langle 1| + |2\rangle\langle 2| - |3\rangle\langle 3| - |4\rangle\langle 4|$ so a positive (negative) δ favors the population of the bottom (top) layer. Without loss of generality, we will consider the case of a positive δ . By reshuffling flavors $|1\rangle, \dots, |4\rangle$, it becomes clear that the magnetic Zeeman term or a population imbalance of orbitals yield the same model Hamiltonian. If $\delta = 0$, the Hamiltonian is SU(4) symmetric. For large δ , the system approaches an effective SU(2) symmetry, where one layer is completely empty and the other half filled.

For later reference, we define observables of the system using the SU(4) generators via $\hat{O}^{ab} = \sum_{\alpha\beta} (\sigma_a \otimes \sigma_b)_{\alpha\beta} S_{\beta}^{\alpha}$, where $a = 0, 1, 2, 3$, with $\sigma_0 = \mathbb{I}_{2 \times 2}$ being the identity matrix and $\sigma_{(1,2,3)} = \sigma^{(x,y,z)}$ the Pauli matrices. Using this notation, the top (bottom) spin operators are given by $\hat{S}_{t(b)}^k = 1/2[\hat{O}^{0,k} + (-) \hat{O}^{3,k}]$, with $k = 1, 2, 3$. Interlayer processes, which define the excitonic order parameter, are encoded by eight operators $\hat{O}^{a,b}$ with $a = 1, 2$ and $b = 0, 1, 2, 3$.

III. THE CLASSICAL GROUND STATE

We first determine the mean-field phase diagram as function of J' and δ and consider the role of quantum fluctuations in the next section. In the SU(4) limit $\delta = 0$ and for $J' = 0$, the classical GS is extensively degenerate: any state with different flavors on neighboring sites minimizes the energy. A finite J' selects a four-sublattice GS out of this manifold [72]. Similarly, at $J' = 0$, we expect an infinitesimal field δ to select a three-sublattice state out of the manifold because

it possesses the maximal polarization $|P_z| = 1/3$ (see Fig. 1). The three-sublattice state with $|P_z| = 1/3$ is still extensively degenerate because any site of the third sublattice can be spin up or down. When $|P_z| < 1/3$, the GS keeps being highly degenerate and can be obtained starting from the three-sublattice state by substituting, e.g., flavors 3 or 4 with flavors 2 or 1 with the constraints of always having different flavors on neighboring sites, as shown in Fig. 1. In the SU(2) limit for large polarization $\delta/J \gg 1$, the effective half-filled triangular lattice possesses 120° antiferromagnetic order for small J' and transitions to a stripe phase for $J' > 1/8$ [24,25].

To obtain the mean-field phase diagram for general δ between these limits, we perform a product state ansatz $|\Psi\rangle = \prod_i |\psi_i\rangle_i$ and minimize the classical energy $E_{\text{cl}} = \langle \Psi | H | \Psi \rangle$ [76]. As an ansatz, we choose a state with in-plane spin order and homogeneous layer polarization P_z given by $|\psi_i\rangle = \frac{\sqrt{1+P_z}}{2}(|1\rangle + e^{iQ'_s \cdot R_i} |2\rangle) + e^{iQ_p \cdot R_i} \frac{\sqrt{1-P_z}}{2}(|3\rangle + e^{iQ'_s \cdot R_i} |4\rangle)$, where Q_p , Q'_s , and Q_s are, respectively, the wave vectors associated with the relative modulations of the pseudospin (layer), bottom spin, and top spin. We choose this ansatz $|\psi_i\rangle$ because it can interpolate between the limiting cases and because it has lower energy than states with flavor-polarized sites (see below). With this ansatz, we can show analytically that for almost complete polarization $|P_z| \lesssim 1$, the GS to order $O((1 - |P_z|)^2)$ is given by a configuration $Q'_s = \Gamma$ and $Q_s = Q_p = K$ (see Appendix A). This describes FM order of the top spin in the scarcely populated layer, and tripartite 120° order of the bottom spin in the densely populated layer, which reduces to the conventional 120° AFM order in the SU(2) limit. Simultaneously, we have a four-component interlayer excitonic order parameter, where the nonvanishing components are given by $\hat{O}^{1,0}$, $\hat{O}^{2,3}$, $\hat{O}^{1,1}$, $\hat{O}^{1,2}$. The pairs $(\hat{O}^{1,0}, \hat{O}^{2,3})$ and $(\hat{O}^{1,1}, \hat{O}^{1,2})$ also form a 120° configuration. At $P_z = 1/3$, the tripartite ΓKK state with homogeneous polarization is degenerate with the manifold of the three-sublattice state with flavor-polarized sites. But for increasing $|P_z|$, the energy of the ΓKK state remains minimal $O((|P_z| - 1/3)^2 J)$, while the energy of the flavor-polarized state rises strongly $O(J)$ (see right panel of Fig. 1).

Our numerical minimization confirms the analytical considerations and allows us to obtain the full mean-field phase diagram between limiting cases. In total, we find three broken-symmetry states divided by two critical lines δ_{c_1} and δ_{c_2} (see Fig. 2). For values of the field $\delta < \delta_{c_1}$ or $J'/J > 1/8$, the energy is minimized by the wave-vector triplet $Q'_s = Q_s = M_1$ and $Q_p = M_2$ (and those related to this by symmetry). This gives rise to a four-sublattice order where top and bottom spin $\hat{S}_{t,b}$ form the same stripe arrangement in one lattice direction given by M_1 , and the interlayer exciton has two components $\hat{O}^{1,0}$ and $\hat{O}^{1,1}$, forming stripes in the other lattice directions defined, respectively, by M_2 and M_3 . This four-sublattice order is reduced to stripes in the SU(2) limit for $J' > 1/8$ [24,25] and recovers the SU(4)-symmetric case at $\delta = 0$ [72]. When $\delta > \delta_{c_2}$, the GS is determined by the tripartite ΓKK state. For $\delta_{c_1} < \delta < \delta_{c_2}$, we find a third GS with triplets of incommensurate wave vectors. The incommensurate order is classically stable for $J'/J \lesssim 0.11$.

For further characterization, we calculate the layer polarization as a function of the external field δ for different values of the NNN exchange intensity J' (see Fig. 2). In

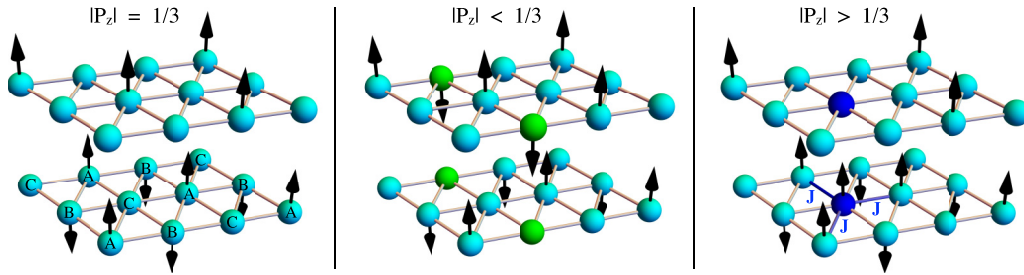


FIG. 1. Sketch of different flavor configurations for $J' = 0$ and three values of the layer polarization. We consider the realization for the four flavors in moiré TMDs as an example and identify $|1\rangle = |\uparrow t\rangle$, $|2\rangle = |\downarrow t\rangle$, $|3\rangle = |\uparrow b\rangle$, $|4\rangle = |\downarrow b\rangle$ for \uparrow/\downarrow spin and t(op)/b(ottom) layer. At zero field, the energy is minimized by any configuration with unequal nearest neighbours. Left: For an infinitesimal field, such degenerate, optimal configurations can be maintained while maximizing the energy gain from the field when $|P_z| = 1/3$. A possible optimal configuration is given by a tripartite order where the A, B, C sublattices are completely polarized, respectively, with states $|\uparrow b\rangle$, $|\downarrow b\rangle$, and $|\uparrow t\rangle$, and where state $|\downarrow t\rangle$ is excluded. Flipping $|\uparrow t\rangle \rightarrow |\downarrow t\rangle$ randomly at any site leaves the energy unchanged. Center: Possible optimal configuration for $|P_z| < 1/3$ obtained from the previous tripartite order where in two sites (highlighted in green) states $|\uparrow b\rangle$ or $|\downarrow b\rangle$ have been flipped into $|\downarrow t\rangle$. Right: High-energy state ($3J$) with nonhomogeneous polarization obtained from the tripartite order by flipping at one site (highlighted in blue) state $|\uparrow t\rangle$ into $|\uparrow b\rangle$.

the four-sublattice state, the polarization increases linearly as a function of the field $|P_z| = \delta/[2(J + J')]$ either until full polarization if $J'/J > 1/8$ or until $\delta = \delta_{c_1}$, where it jumps abruptly to a higher value and the order becomes tripartite (if $0.11 \lesssim J'/J < 1/8$) or incommensurate (if $J'/J \lesssim 0.11$). In the incommensurate phase, the polarization has a non-linear behavior for $\delta_{c_1} < \delta < \delta_{c_2}$, and at $\delta = \delta_{c_2}$ the system continuously transitions into the tripartite phase. In the tripartite phase, the polarization increases linearly as $|P_z| = (8/27)\delta/J + 1/3$. We evaluate the size of the first-order jump using Maxwell's construction (see Fig. 2), which displays a nonmonotonic behavior as a function of J' . At $J' = 0$ the polarization jumps at $\delta = 0^+$ from zero to $|P_z| = 1/3$. In approaching this point, the slope of the polarization in the incommensurate region becomes steeper with decreasing J'

so the layer polarizability $\kappa = \frac{dP_z}{d\delta}$ diverges at $J' = 0$. Such an instability of the incommensurate order is accompanied by the onset of a continuous manifold of degenerate GSs for the classically forbidden values of the polarization $|P_z| < 1/3$ [77]. It is characterized by Q-vector triplets defined on three curves $Q'_s(\theta)$, $Q_s^b(\theta)$, $Q_p(\theta)$ around Γ and K (K') in the Brillouin zone parameterized by the angle θ as shown in Fig. 2 for the representative case of $|P_z| = 0.183$.

IV. THE ROLE OF QUANTUM FLUCTUATIONS

We study the excitation spectrum and the stability of the different phases within flavor-wave theory. Before adding quantum fluctuations to the mean-field solution, it is useful to introduce a unitary transformation \mathcal{U}_i that brings $|\psi_i\rangle \rightarrow |1\rangle$,

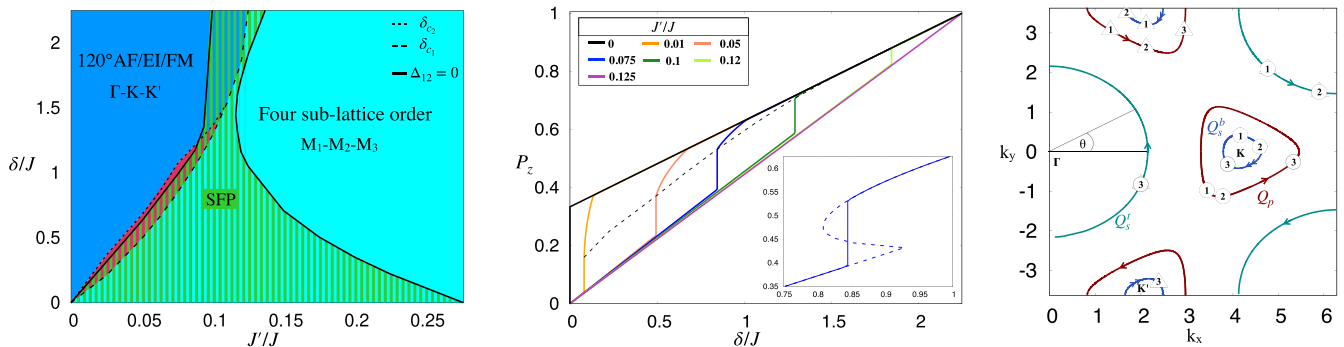


FIG. 2. Left: Phase diagram in the plane δ vs J' within mean field (dashed lines δ_{c_1} and δ_{c_2}) and including quantum fluctuations (solid lines). We find three phases displaying long-range order which we label with the wave-vector triplet Q'_s , Q_p , $Q_s^b + Q_p$ (see text). The blue Γ - K - K' regime describes 120° spin (AFM) and exciton order (EI) with minority ferromagnetism (FM). In the turquoise M_1 - M_2 - M_3 region, spin and excitons form stripes in each layer, leading to a four-sublattice order, and in the red region, they order with incommensurate wave vectors. The green area in the phase diagram that we named the strongly fluctuating phase (SFP) indicates the region where quantum fluctuations suppress the order parameter Δ_{12} to zero. It connects candidate spin liquids of the $SU(2)$ ($\delta/J \gg 1$) and $SU(4)$ ($\delta = 0$) limit. Vertical blue, turquoise, and red hatches refer, respectively, to the Γ - K - K' / M_1 - M_2 - M_3 incommensurate orders predicted by mean-field theory that are suppressed by quantum corrections. Center: Mean-field polarization curves as a function of the external field for different values of J'/J . The inset shows the Maxwell construction for $J'/J = 0.075$. Dashed line is a guide to the eye for the first-order jump. Right: Ground-state degenerate manifold for $|P_z| = 0.183 < 1/3$ given by three different curves made of Q-vector triplets Q'_s (green), Q_s^b (blue), and Q_p (red) that minimize the classical energy. We explicitly mark three examples of triplets ($Q'_s(n)$, $Q_s^b(n)$, $Q_p(n)$) numbered by $n = 1, 2, 3$. States with Q_s^b , Q_p around K (circles) and K' (triangles) are degenerate. Arrows denote how triplets evolve with θ , accounting for double valued $Q_s^b(\theta + \pi; K^{(\prime)}) = Q_s^b(\theta; K^{(\prime)})$.

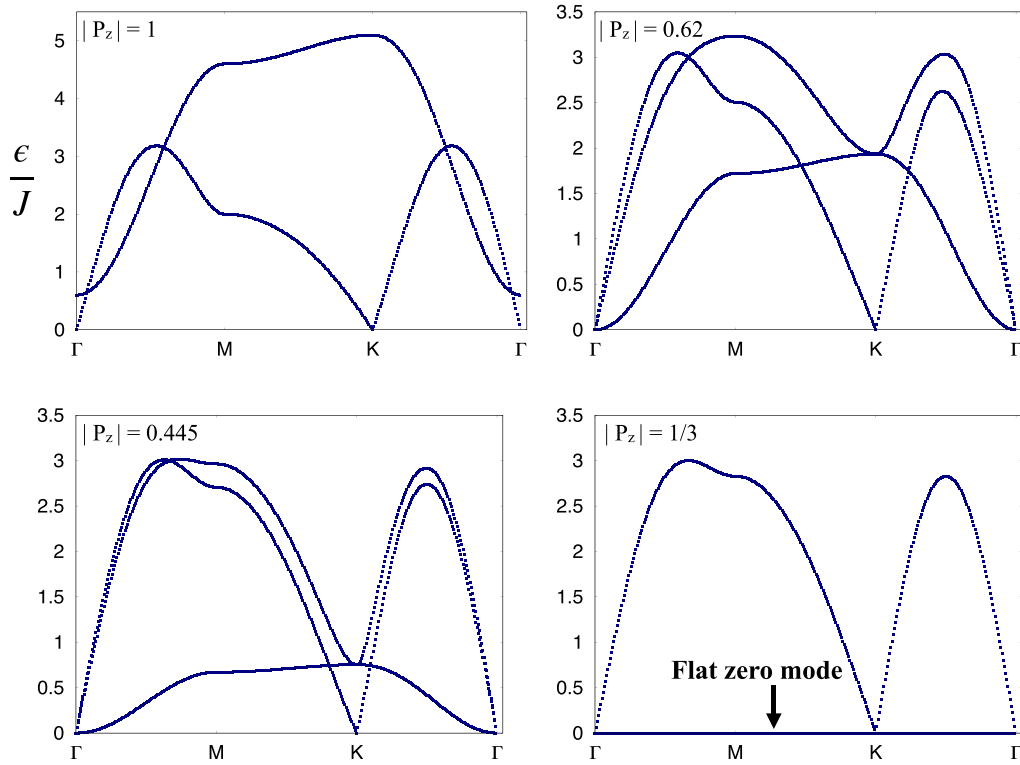


FIG. 3. Evolution of the flavor-wave spectrum plotted as a function of the crystalline momentum for different values of the layer polarization $|P_z| = 1, 0.62, 0.445, 1/3$.

in the same spirit as has been done for evaluating the spin waves of the 120° AFM [78] and the nonhomogenous quantum Ising model [79]. In this new basis, the GS assumes the form of a homogeneous fully polarized state where every site is in the state $|1\rangle$. The Hamiltonian in the new basis reads

$$\begin{aligned} \mathcal{U} H \mathcal{U}^\dagger = & \sum_{ij} \sum_{\alpha\alpha'\beta\beta'} J(\tau) \kappa_{\alpha\alpha'}(\tau) \kappa_{\beta\beta'}^*(\tau) S_\beta^\alpha(i) S_{\alpha'}^{\beta'}(j) \\ & + \delta \sum_i \sum_{\alpha\beta} \tilde{P}_{\alpha\beta}^z S_\beta^\alpha(i), \end{aligned} \quad (2)$$

where $\kappa_{\alpha\beta}(\tau) = \langle \alpha | \mathcal{U}_i \mathcal{U}_j^\dagger | \beta \rangle$, with $\tau = R_i - R_j$, and $\tilde{P}_{\alpha\beta}^z = \langle \alpha | \mathcal{U}_i \hat{P}_i^z \mathcal{U}_i^\dagger | \beta \rangle$. We rewrite the Hamiltonian in Eq. (2) as $E_{\text{cl}} + \delta H$, where δH contains the quantum fluctuations in terms of a generalized Holstein-Primakoff transformation $S_1^1 = M - \sum_n b_n^\dagger b_n$, $S_m^1 = b_m \sqrt{M - \sum_n b_n^\dagger b_n}$, and $S_m^n = b_n^\dagger b_m$ with three bosonic operators $b_n^{(\dagger)}$, $n \in \{1, 2, 3\}$, and expansion in $1/M$. In the harmonic approximation, we can calculate the characteristic flavor-wave spectrum for the different phases by diagonalizing δH for various values of δ and J' . We also explicitly checked that the dynamical structure factors contain the same excitations (see Appendix B 2). We first discuss the results at $J' = 0$. In Fig. 3, we show four different spectra as a function of the crystalline momentum for different values of the polarization greater than $1/3$. For large enough values of δ , when the system is fully polarized $|P_z| = 1$, the spin waves of the half-filled bottom layer coincide with the ones of the monolayer 120° AFM [24,25,78,80]. They are gapless at $k = \Gamma, K$ and their energy increases linearly in the vicinity of those points. On top of these excitations, we find two degenerate

gapped FM-like spin waves, which encode the hopping of one electron from the bottom to the top layer. Their gap at the Γ point is controlled by $2|\delta - \delta_s|$ for $\delta > \delta_s$, where $\delta_s = 9/4J$ is the minimum value of the field necessary for full polarization. For intermediate values of $|P_z|$ lying in the interval $(1/3, 1)$, we have three distinct Goldstone modes at the Γ point, two of which have a linear dispersion with different velocities while the third one displays a quadratic behavior that is associated to the FM $Q_s^1 = 0$ wave vector of the top-layer spin order. At the K point, we observe only one linear Goldstone mode. Furthermore, the FM mode is strongly suppressed by decreasing the polarization toward the critical value of $1/3$. At the same time, the two other branches approach each other. At the critical point $|P_z| = 1/3$, we obtain two degenerate excitations with linear Goldstone modes at the Γ and K points, and the FM mode completely flattens to zero. As mentioned before, these zero-energy excitations are already present in the classical picture, where any spin in the minority layer of the state with flavor-polarized sites can be flipped without energy cost, and we observe that they survive upon inclusion of Gaussian quantum fluctuations. They strongly affect the system's properties and mark the end of long-range order that for $J' = 0$ is stable up to $|P_z| = 1/3$.

It is also instructive to analyze the role of quantum fluctuations in the classically forbidden region of the parameter space $|P_z| < 1/3$. In this region, the classical GS is highly degenerate. However, quantum fluctuations can remove such a high degeneracy and select particular states which become energetically favored once quantum corrections are taken into account, a well known phenomenon known as quantum order-by-disorder [81–85]. To determine the GS, we

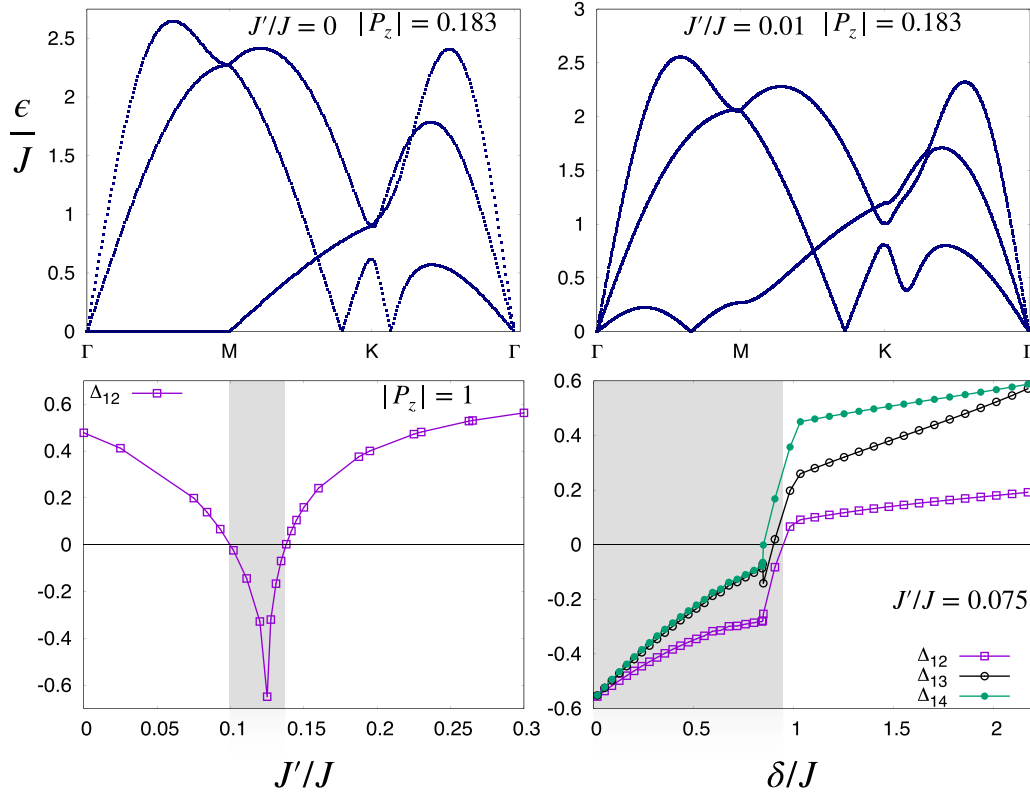


FIG. 4. Top panels: Flavor-wave spectra for $|P_z| = 0.183$ and two different values of $J'/J = 0, 0.01$. Lower left: Renormalized order parameter as a function of J'/J at full polarization. Lower right: Order parameter components as a function of the external field for fixed $J'/J = 0.075$. When $\Delta_{1\alpha} < 0$ (gray shaded area in the plots), quantum fluctuations destroy the mean-field order.

calculate quantum corrections to the energy for every degenerate classical state by evaluating the zero-point energy of quantum fluctuations (see Appendix B 1). We find that Q_s^a and Q_s^b selected by quantum fluctuations lie, respectively, on the Γ - M and K - M directions. Figure 4 displays the flavor-wave spectrum as a function of the crystalline momentum for $P_z = -0.183$. We observe that the fluctuation energy vanishes along the Γ - M direction and that we have Goldstone modes at the M point and at two incommensurate wave vectors lying, respectively, on the M - K and K - Γ directions. The nodal line in the Γ - M direction is again a consequence of the high degeneracy of the classical GS and disorders the system. As we show below, the presence and proximity of the zero modes strongly renormalizes the order parameter and suppresses it to zero in large parts of the phase diagram.

When J' is finite, the degeneracy of the classical GS is removed everywhere in the phase diagram even in the case of incommensurate order. Figure 4 shows the flavor-wave spectra for $J'/J = 0.01$ and $|P_z| = 0.183$. We find that even small values of the NNN superexchange are enough to remove the nodal lines appearing in the classically forbidden region at $J' = 0$. Furthermore, we observe that the Goldstone mode appearing at the M point for $J' = 0$ now shifts to an incommensurate vector lying in the Γ - M direction, and that the extra Goldstone mode appearing along $\Gamma - K$ for $J' = 0$ acquires a gap.

The regularization of the spectra introduced by a non-vanishing J' allows us to quantify the impact of quantum

fluctuations on the order parameter and map out the phase diagram beyond the mean-field approximation. The classical GS in the new basis defined in Eq. (2) is given by the completely polarized state $\prod_i |1\rangle_i$, with $n_1 = 1$ and $n_2 = n_3 = n_4 = 0$, where $n_\alpha = \frac{1}{V} \sum_i \langle S_\alpha^\alpha(i) \rangle$ is the α th flavor population. With the inclusion of quantum fluctuations, the density matrix $n_{\alpha\beta} = \frac{1}{V} \sum_i \langle S_\beta^\alpha(i) \rangle$ acquires off-diagonal terms and has a block-diagonal form given by a 1×1 ($\alpha, \beta = 1$) and a 3×3 ($\alpha, \beta \in \{2, 3, 4\}$) block (see Appendix B). Then, it is natural to choose the basis that diagonalizes the density matrix. The eigenvalues are the occupation numbers of the minority flavors that, for simplicity, we still refer to as n_2, n_3 , and n_4 , and we sort in descending order, i.e., $n_2 > n_3 > n_4$. The population of the majority flavor can be computed from the knowledge of the renormalized minority ones via $n_1 = 1 - \sum_{\alpha=2}^4 n_\alpha$. In the generic case, the four occupation numbers are nonvanishing and we can express the order parameter in terms of three components $\Delta_{1\alpha} = n_1 - n_\alpha$ with $\alpha = 2, 3, 4$. We identify the region in the phase diagram enclosed by the contour $\Delta_{12} = 0$ (see Fig. 2) as a SFP, where quantum fluctuations are so strong that n_1 does not represent the occupation of the majority flavors anymore [86].

The lower panels of Fig. 4 show the order parameter $\Delta_{1\alpha}$ as a function of NNN superexchange and polarization. As we explained before, at $|P_z| = 1$ we have a fully polarized layer with one fermion per site, which is equivalent to the $SU(2)$ Heisenberg model. In this case, the GS transitions from a 120° AFM to a striped phase at $J'/J = 1/8$ on the mean-field level

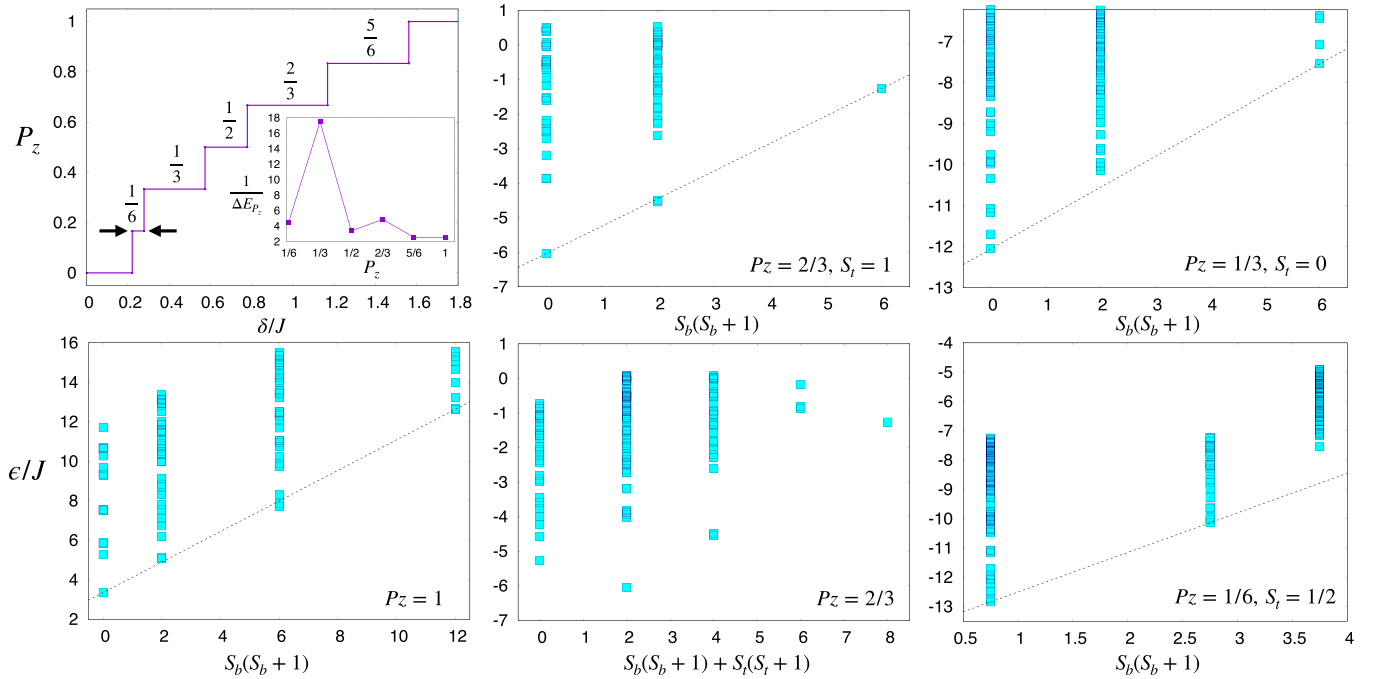


FIG. 5. Numerical results from Lanczos exact diagonalization. Left top: Polarization as a function of the external field. The inset displays the inverse of the plateaux width as a function of polarization, which is an estimate of the system’s polarizability (see main text). The other panels show the low-energy eigenspectra of the Hamiltonian belonging to different polarization sectors. Antiferromagnets form the Anderson tower of states proportional to S^2/N . Dashed lines are guide to the eyes.

[24,25]. We note that the occupation numbers $n_3 = n_4 = 0$ in the SU(2) limit, and the order parameter has only one component, Δ_{12} . It displays a cusp at the transition point $J'/J = 1/8$ and crosses zero at two different close-by points, namely, $J'_a/J \approx 0.1$ and $J'_b/J \approx 0.138$. Between these points $J_a < J' < J_b$, the order parameter vanishes and becomes negative. This means that the harmonic approximation cannot be trusted anymore because quantum fluctuations are so strong to the point of destroying the order parameter. Interestingly, this interval is quantitatively comparable to the range of values where a spin-liquid phase was predicted by Monte Carlo [30,34] and density matrix renormalisation group (DMRG) [27,28] calculations.

As an example, we also show the occupation numbers as a function of the external field at fixed $J'/J = 0.075$ in Fig. 4. For values of P_z close to complete polarization, the system is in the Γ - K - K phase and we find $n_4 = 0$, so $n_1 = \Delta_{14}$ only mildly decreases as a function of decreasing δ . At $\delta \sim J$, the GS becomes incommensurate, $n_4 > 0$ and all $\Delta_{1\alpha}$ are lowered quite rapidly by decreasing δ crossing zero ($\Delta_{1\alpha} = 0$) thereafter within the incommensurate phase. For smaller values of δ , the harmonic approximation breaks down and the system enters the strongly fluctuating regime.

We summarize the impact of quantum fluctuations in the phase diagram in Fig. 2. We observe that the strongly fluctuating regime connects the putative spin liquid phases of the SU(4) and SU(2) limits when the layer population is varied with δ . Similarly, for larger J' the four-sublattice and stripe phases of the limiting cases are continuously connected. In contrast, the Γ KK phase, which reduces to the 120° AFM for full polarization, is destroyed by strong fluctuations before the SU(4) $\delta = 0$ limit can be reached. For small J'/J the strongly

fluctuating regime is preempted by an incommensurate phase.

V. EXACT SPECTRA

To gain additional insights about the underlying physics of the exact solution, we perform Lanczos exact diagonalization for a 12-site cluster with periodic boundary conditions defined by the lattice vectors $T_1 = 4a_2 - 2a_1$ and $T_2 = 2a_1 + 2a_2$, where $a_1 = (1, 0)$ and $a_2 = \frac{1}{2}(1, \sqrt{3})$. In Fig. 5, we show the polarization as a function of the external field. The finite size allows for seven different polarization values, namely, $P_z = 1, 5/6, 2/3, 1/2, 1/3, 1/6, 0$. Therefore, the polarization displays seven plateaux. The width of a given plateau matches the energy difference between the two GSs belonging to the two different polarization sectors, i.e., $\Delta E_{P_z} = E_{0,P_z} - E_{0,P_z-1/6}$. In the thermodynamic limit, the layer polarizability is given by $\kappa = (\lim_{\Delta P_z \rightarrow 0} \frac{\Delta E_{P_z}}{\Delta P_z})^{-1}$. Hence, we can use the finite difference ΔE_{P_z} as an approximate estimate of the inverse layer polarizability (see inset in Fig. 5). We observe that $\Delta E_{P_z}^{-1}$ is strongly peaked at $P_z = 1/3$, where its value is one order of magnitude larger than for the other polarizations. This is in line with the sharpening of the slope of the polarization upon approaching $|P_z| = 1/3$ in the mean-field calculation (Fig. 2).

Further insights about the tendency of the system to stabilize a long-range order can be gained by studying the low-energy sector of the energy eigenspectrum. Mean-field theory plus quantum fluctuations suggest that the bottom (top) layer orders antiferromagnetically (ferromagnetically) for $P_z \geq 1/3$. We can check the tendency of the system to form an AFM order in the bottom layer by plotting the en-

ergy eigenvalues as a function of the total spin of the bottom layer, i.e., $S_b^2 = (S_{b,\text{tot}}^x)^2 + (S_{b,\text{tot}}^y)^2 + (S_{b,\text{tot}}^z)^2$, with $S_{b,\text{tot}}^{(x,y,z)} = \sum_i S_b^{(x,y,z)}(i)$, which is a conserved quantity. In fact, the low-energy eigenstates of AFMs form a structure known as the Anderson tower of states: well-separated states that are proportional to S^2/N [72,87–90]. On the other hand, ferromagnets do not display the same behavior. Therefore, for $P_z \geq 1/3$, we expect the spectrum to only form the Anderson tower when the energy eigenvalues are plotted as a function of S_b^2 , and not when it is plotted as a function of the total spin. In Fig. 5, we show the energy spectra for different values of the polarization sectors. For $P_z = 1$, the spectrum of the bottom layer reproduces the one of the SU(2)-Heisenberg model [88]. At $P_z = 2/3$, the GS is found in the sector with $S_b = 0$ and $S_t = 1$: we observe that the low-energy excited states with $S_t = 1$ show a linear behavior as a function of $S_b(S_b + 1)$. However, when the spectrum is plotted as a function of the total spin eigenvalues, the linear behavior is lost as expected. Furthermore, the GS is found in the maximal spin sector of the top layer, signaling the tendency towards a FM order in the top layer. At $P_z = 1/3$, we start to observe a small deviation from linear behavior of the spectrum as a function of $S_b(S_b + 1)$. Furthermore, we now find the GS in the minimal top-layer spin sector, i.e., $S_t = 0$, probably suggesting that FM order is already lost for this value of the polarization. At $P_z = 1/6$, we observe a sizable deviation from linear behavior, suggesting that at this value of the polarization, the bottom layer does not order antiferromagnetically. Thus, the results of the exact diagonalization provide strong indication that the GS is quantum disordered for small enough polarizations.

VI. CONCLUSIONS

Motivated by realizations in cold atoms and moiré TMDs, we carried out a theoretical study of the paradigmatic SU(4)-Heisenberg model on the triangular lattice in the presence of a polarizing field δ , which controls a population imbalance of of flavor pairs. On the classical level, the model is strongly frustrated with an extensive GS degeneracy, which we argued can persist for finite fields up to polarizations $|P_z| \leq 1/3$. Through a combination of variational mean-field calculations, flavor-wave theory, and exact diagonalization, we determined the GSs and excitation spectra for different values of the field δ and NN coupling J' . We mapped out a rich phase diagram with commensurate and incommensurate long-range orders, as well as a SFP that shows evidence for a quantum disordered GS.

For small J'/J and large enough δ , we found a tripartite phase where the bottom-layer spin and the interlayer exciton order in a 120° fashion while the top layer is ferromagnetically ordered. Accordingly, its flavor-wave spectrum shows AFM and FM excitations. For large J'/J , we found a four-sublattice phase for all values of δ which displays a striped configuration for top spin, bottom spin, and excitonic order parameter. In between these two phases, we found a small sliver of incommensurate order and a large regime of a SFP where quantum fluctuations suppress long-range order. This is mirrored by extended zero modes in the flavor-wave spectrum for $J' \rightarrow 0$. Our ED calculations on a 12-site cluster provided supporting

evidence for a transition from an ordered to a disordered phase between large and small values of the polarization. Furthermore, we observed a strong increase in the polarizability upon approaching the transition.

We argued that in the case of full polarization, where the system effectively models the SU(2)-symmetric triangular lattice, the SFP can be identified as the precursor of the spin liquid state found in DMRG and Monte Carlo calculations [27,28,30,34,35]. Similarly, the SFP coincides with a putative quantum liquid in the SU(4) limit $\delta = 0$ [19,22,69]. Interestingly, the two limits are continuously connected via the SFP, making future studies on possible liquid phases in this regime highly desirable. This could also shed new light on the debated nature of the SU(2) quantum spin liquid.

Given the rich phase structure, spin and charge configurations can be effectively manipulated via the external field. The tunability of cold-atom and moiré systems provides an ideal opportunity to investigate these quantum many-body phases experimentally. The polarizing field can be readily controlled and the NNN exchange J' is not expected to be very large, so it seems possible to reach the SFP regime, in particular, because it occupies an extended region of the phase space. For example, the softening of the FM mode, which could be probed by measuring the dynamic structure factor (see Appendix B 2), would yield direct evidence of approaching the SFP. Intriguingly, a recent experiment on twisted AB-stacked WSe₂ reported evidence for paramagnetic insulators at hole density $n = 1$ for zero and full polarization, and a potential EI for intermediate polarization. While this is in accordance with our findings, further experimental and theoretical investigations are needed to elucidate the nature of the insulating states. Most notably, this includes the possible emergence of Mott insulators in the associated Hubbard model.

ACKNOWLEDGMENTS

We thank M. Capone, A. Amaricci, E. König, M. Knap, J. Knolle, F. Pollmann, and T. Schäfer for valuable discussions.

APPENDIX A: CLASSICAL ENERGY IN LIMITING CASES

The explicit expression for the classical energy $E_{cl} = \langle \Psi | H | \Psi \rangle$ using the product state ansatz $|\Psi\rangle = \prod_i |\psi_i\rangle_i$ with $|\psi_i\rangle = \frac{\sqrt{1+P_z}}{2}(|1\rangle + e^{iQ'_s R_i} |2\rangle) + e^{iQ_p R_i} \frac{\sqrt{1-P_z}}{2}(|3\rangle + e^{iQ'_s R_i} |4\rangle)$ is given by

$$E_{cl} = E_J + E_{J'} + E_\delta, \quad (\text{A1})$$

$$\begin{aligned} \frac{1}{JN} E_J &= \frac{3}{2} (1 + P_z^2) + \frac{1}{4} \sum_{\tau=1}^3 ((1 + P_z)^2 \cos Q'_s \tau \\ &\quad + (1 - P_z)^2 \cos Q'_s \tau + (1 - P_z^2) [\cos Q_p \tau \\ &\quad + \cos (Q_p + Q'_s) \tau + \cos (Q_p - Q'_s) \tau \\ &\quad + \cos (Q_p + Q'_s - Q'_s) \tau]), \end{aligned} \quad (\text{A2})$$

$$\begin{aligned} \frac{1}{J'N} E_{J'} &= \frac{3}{2} (1 + P_z^2) + \frac{1}{4} \sum_{\rho=1}^3 ((1 + P_z)^2 \cos Q'_s \rho \\ &\quad + (1 - P_z)^2 \cos Q'_s \rho + (1 - P_z^2) [\cos Q_p \rho \end{aligned}$$

$$+ \cos(Q_p + Q_s^b)\rho + \cos(Q_p - Q_s^t)\rho + \cos(Q_p + Q_s^b - Q_s^t)\rho] \quad (\text{A3})$$

$$\frac{1}{N}E_\delta = \delta P_z, \quad (\text{A4})$$

where $P_z = \langle \psi | \hat{P}_z | \psi \rangle$, and τ (ρ) are (N)NN vectors of the triangular lattice. Generally, the NN sums are minimized by $Q_i = \pm K$ with $\sum_{\tau=1}^3 \cos K\tau = -3/2$, while NNN sums prefer any of the three M vectors $Q_i = M$ since $\sum_{\rho=1}^3 \cos M\rho = -1$ while $\sum_{\rho=1}^3 \cos K\rho = 3$ and $\sum_{\tau=1}^3 \cos M\tau = -1$.

When δ is large, so $P_z \rightarrow -1$, the leading order terms $\propto (1 - P_z)^2 = O(1)$ of NN and NNN sums compete. They become equal $(E_J + E_{J'})_{Q_s^b=K} = (E_J + E_{J'})_{Q_s^b=M}$ when $J'/J = 1/8$ reproducing the mean-field transition from 120° AFM to stripe phase in the SU(2) case.

Thus, when we consider the case of $J' = 0$ in the $P_z \rightarrow -1$ limit, we obtain $Q_s^b = K$. Then, the next-to-leading order terms $\propto (1 - P_z^2) = O((1 + P_z))$ can all be simultaneously minimized by the configuration $Q_p = K$ and $Q_s^t = 0$, which is the tripartite state we describe in the main text. The total energy of this state is $E_J/(NJ) = 3(1 - 3P_z)^2/8$, where N is the number of lattice sites. This becomes degenerate $E_J = 0$ with the manifold of three-sublattice states that have flavor-polarized sites at $P_z = 1/3$. However, to slightly increase $P_z \gtrsim 1/3$ in the latter state, an energy of order J is needed to flip one site from top to bottom layer. In contrast, the energy cost of the homogeneous configuration is much smaller $(1 - 3P_z)^2 \ll 1$.

Considering $J'/J > 1/8$ next, the leading order term fixes $Q_s^b = M$. It is again possible to minimize all second-order terms $O((1 + P_z))$ via $Q_s^t = M$ and $Q_p = M'$, where M and M' are two inequivalent M vectors. The energy of this homogeneous four-sublattice state is $(E_J + E_{J'})/N = 2(J + J')P_z^2$, which becomes degenerate with the four-sublattice states with flavor-polarized sites in the SU(4) limit $P_z \rightarrow 0$.

APPENDIX B: INCLUSION OF QUANTUM FLUCTUATIONS

We shall assume that, after the unitary transformation, the GS of Eq. (2) is very close to the fully polarized state $\prod_i |1\rangle_i$. Hence, we can use the following approximation [72,76,91] for the operators:

$$\begin{aligned} S_1^1(i) &\sim M - \sum_{\alpha \neq 1} b_\alpha^\dagger(i) b_\alpha(i), \\ S_\alpha^1(i) &\sim \sqrt{M} b_\alpha^\dagger(i), \quad (\text{with } \alpha \neq 1), \\ S_\beta^\alpha(i) &\sim b_\beta^\dagger(i) b_\alpha(i), \quad (\text{with } \alpha, \beta \neq 1), \end{aligned} \quad (\text{B1})$$

where $b_\alpha^\dagger(i)$ and $b_\alpha(i)$ are creation and annihilation operators following bosonic statistics, i.e., $[b_\alpha(i), b_\beta^\dagger(j)] = \delta_{ij}\delta_{\alpha\beta}$ and M is the classical expectation value of S_1^1 . Substituting Eq. (B1) in Eq. (2), we have

$$\mathcal{U}H\mathcal{U}^\dagger = H_0 + H_1 + H_2 + \dots, \quad (\text{B2})$$

where H_n contains bosonic operators to the power of n . Within the harmonic approximation we truncate the series in Eq. (B2) to the second order. The first term in the expansion

gives back the classical energy which reads

$$H_0 = NM^2 \frac{1}{2} \sum_\tau J(\tau) |\kappa_{11}(\tau)|^2 + NM\delta\tilde{P}_{11}^z. \quad (\text{B3})$$

It is clear from the last equation that δ must be proportional to M to be consistent with Eq. (B1).

The second term in the expansion contains linear terms in the bosonic fields and reads

$$\begin{aligned} H_1 &= M^{\frac{3}{2}}N \sum_{\alpha \neq 1} \sum_\tau \frac{J(\tau)}{2} (\kappa_{11}\kappa_{1\alpha}^\dagger + \kappa_{\alpha 1}\kappa_{11}^\dagger) b_\alpha(i) + \text{H.c.} \\ &+ \delta N\sqrt{M} \sum_{\alpha \neq 1} \tilde{P}_{\alpha 1}^z b_\alpha(i) + \text{H.c.} \end{aligned} \quad (\text{B4})$$

This term must vanish for stability reasons and this condition fixes the value of δ that, after we set $M = 1$, reads

$$\delta = - \frac{\sum_\tau J(\tau) \text{Re} \kappa_{11}(\tau) \kappa_{1\alpha}^\dagger(\tau)}{\tilde{P}_{1\alpha}^z}. \quad (\text{B5})$$

It is worth noting that the quantity on the right-hand side of Eq. (B5) does not depend on the index α for symmetry reasons.

After setting $M = 1$, the quadratic term reads

$$\begin{aligned} H_2 &= \sum_i \left(- \sum_\tau J(\tau) |\kappa_{11}|^2 - \delta\tilde{P}_{11}^z \right) \sum_\alpha b_\alpha^\dagger(i) b_\alpha(i) \\ &+ \sum_{i\alpha\beta} \left(\sum_\tau J(\tau) \kappa_{\alpha 1} \kappa_{\beta 1}^\dagger + \delta\tilde{P}_{\alpha\beta}^z \right) b_\beta^\dagger(i) b_\alpha(i) \\ &+ \sum_{i\tau\alpha\beta} \frac{J(\tau)}{2} \kappa_{\alpha\beta} \kappa_{11}^\dagger b_\alpha(i) b_\beta^\dagger(i + \tau) + \text{H.c.} \\ &+ \sum_{i\tau\alpha\beta} \frac{J(\tau)}{2} \kappa_{\alpha 1} \kappa_{1\beta}^\dagger b_\alpha(i) b_\beta(i + \tau) + \text{H.c.}, \end{aligned} \quad (\text{B6})$$

where we used the shorthand notation for $b_\alpha(i + \tau)$, which indicates the destruction operator of a boson with flavor α at site $R_i + \tau$. After expanding the bosonic fields in their Fourier components $b_\alpha(i) = \frac{1}{\sqrt{N}} \sum_k e^{ikR_i} b_{k\alpha}$, we can rewrite the quadratic Hamiltonian in momentum space as the following:

$$\begin{aligned} H_2 &= \sum_k \sum_{\alpha\beta} \chi_{\alpha\beta} b_{k\alpha}^\dagger b_{k\beta} + (f_{\alpha\beta}(k) b_{k\alpha} b_{k\beta}^\dagger + \text{H.c.}) \\ &+ \sum_k \sum_{\alpha\beta} g_{\alpha\beta}(k) b_{k\alpha} b_{-k\beta} + \text{H.c.}, \end{aligned} \quad (\text{B7})$$

where

$$\begin{aligned} \chi_{\alpha\beta} &= \sum_\tau J(\tau) \kappa_{\alpha 1} \kappa_{\beta 1}^* + \delta\tilde{P}_{\alpha\beta}^z \\ &- \delta_{\alpha\beta} \left(\sum_\tau J(\tau) |\kappa_{11}|^2 + \delta\tilde{P}_{11}^z \right), \\ f_{\alpha\beta}(k) &= \sum_\tau \frac{J(\tau)}{2} e^{ik\tau} \kappa_{\alpha\beta} \kappa_{11}^*, \\ g_{\alpha\beta}(k) &= \sum_\tau \frac{J(\tau)}{2} e^{-ik\tau} \kappa_{\alpha 1} \kappa_{1\beta}^*. \end{aligned} \quad (\text{B8})$$

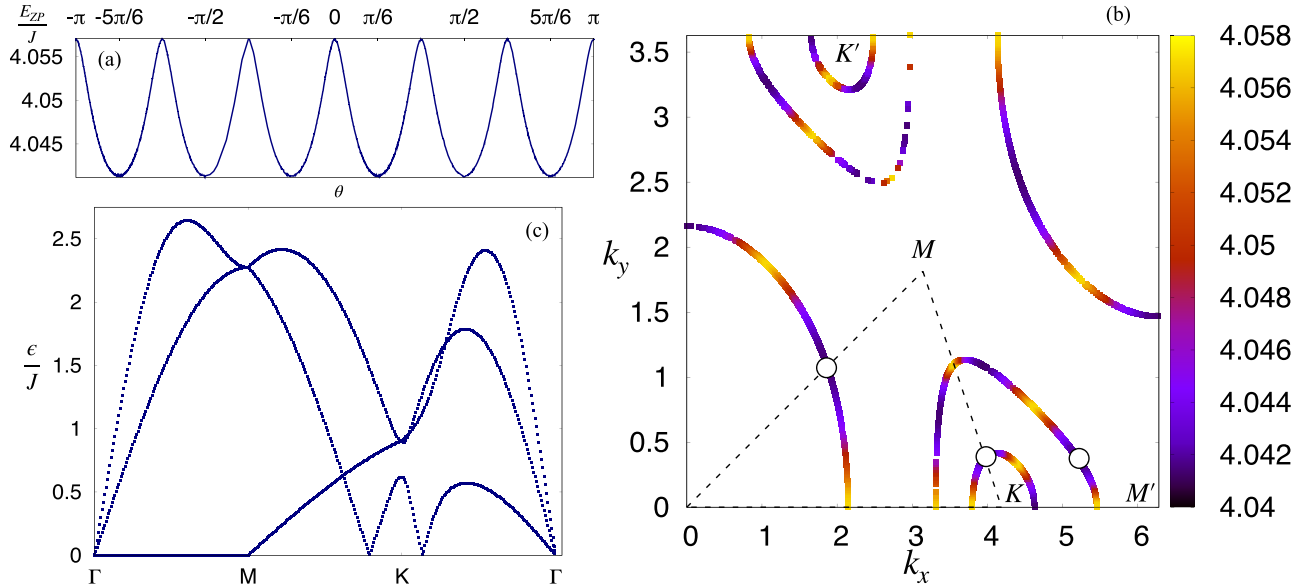


FIG. 6. Quantum fluctuations for $P_z = -0.183$ which lie in the classically forbidden region. (a) Zero-point energy plotted as a function of the polar angle θ . (b) Energy distribution on the classical contours shown in Fig. 2. (c) Spin waves spectrum plotted as a function of the crystalline momentum.

It is useful to introduce the set of conjugate variables $b_{k\alpha} = \frac{1}{\sqrt{2}}(x_{k\alpha} + ip_{k\alpha})$ and $b_{k\alpha}^\dagger = \frac{1}{\sqrt{2}}(x_{-k\alpha} - ip_{-k\alpha})$, which obey the canonical commutation relation $[x_{k\alpha}, p_{k'\alpha'}] = i\delta_{\alpha\alpha'}\delta_{k,-k'}$. After substituting these expressions in Eq. (B7), we can finally write the Hamiltonian in the following matrix form:

$$H_2 = \frac{1}{2} \sum_k \begin{pmatrix} \mathbf{p}_k \\ \mathbf{x}_k \end{pmatrix}^T \begin{bmatrix} \mathcal{H}^P(k) & \mathcal{H}^{PX}(k) \\ \mathcal{H}^{XP}(k) & \mathcal{H}^X(k) \end{bmatrix} \begin{pmatrix} \mathbf{p}_{-k} \\ \mathbf{x}_{-k} \end{pmatrix} + \mathcal{C}, \quad (\text{B9})$$

where $\mathbf{p}_k = (p_{k1}, p_{k2}, p_{k3})$, $\mathbf{x}_k = (x_{k1}, x_{k2}, x_{k3})$, with $x_{k\alpha}$ and $p_{k\alpha}$ being conjugate variables obeying the commutation relation $[x_{k\alpha}, p_{k'\beta}] = i\delta_{k,-k'}\delta_{\alpha\beta}$. The Hamiltonian is a 6×6 matrix that has been represented in a block form in Eq. (B9), where each block represents a 3×3 matrix. In particular, we have that

$$\begin{aligned} \mathcal{H}_{\alpha\beta}^P(k) &= \chi_{\alpha\beta} + f_{\alpha\beta}(k) + f_{\alpha\beta}(-k) + g_{\alpha\beta}(k) + g_{\alpha\beta}(-k) \\ \mathcal{H}_{\alpha\beta}^X(k) &= \chi_{\alpha\beta} + f_{\alpha\beta}(k) + f_{\alpha\beta}(-k) - g_{\alpha\beta}(k) - g_{\alpha\beta}(-k) \\ \mathcal{H}_{\alpha\beta}^{XP}(k) &= i[-f_{\alpha\beta}(k) + f_{\alpha\beta}(-k) + g_{\alpha\beta}(k) - g_{\alpha\beta}(-k)] \\ \mathcal{H}_{\alpha\beta}^{PX}(k) &= [\mathcal{H}_{\alpha\beta}^{XP}(k)]^*. \end{aligned} \quad (\text{B10})$$

The additive constant in Eq. (B9) is given by $\mathcal{C} = -\frac{N}{2} \sum_{\alpha} \chi_{\alpha\alpha}$. The spectrum of the quantum excitations is given by the symplectic spectrum of the Hamiltonian in Eq. (B9), which coincides with the eigenvalues $\epsilon_{k\alpha}$ of $i\mathcal{J}\mathcal{H}(k)$, with $\mathcal{J} = -i\sigma^y \otimes \mathbb{I}_{3 \times 3}$ [92].

Within the harmonic approximation, the expression of the density matrix is given by

$$n_{\alpha\beta} = \left\langle \begin{pmatrix} \mathbf{p}_k \\ \mathbf{x}_k \end{pmatrix}^T \begin{bmatrix} |\alpha\rangle\langle\beta| & i|\alpha\rangle\langle\beta| \\ -i|\alpha\rangle\langle\beta| & |\alpha\rangle\langle\beta| \end{bmatrix} \begin{pmatrix} \mathbf{p}_{-k} \\ \mathbf{x}_{-k} \end{pmatrix} \right\rangle_{\text{BZ}}, \quad (\text{B11})$$

where $\alpha, \beta = 2, 3, 4$ and the subscript BZ means that the quantum expectation values for the different crystalline

momenta must be averaged over the Brillouin zone. The expectation value of the majority flavors, according to Eq. (B1), is then given by $n_1 = 1 - \sum_{\alpha=2}^4 n_{\alpha\alpha}$.

1. Order by disorder

Quantum fluctuations can remove the high degeneracy of the classical GS in the regime $|P_z| < 1/3$ and select particular states. To investigate this quantum order-by-disorder phenomenon [81–85], we calculate quantum corrections to the energy for every degenerate classical state. This is done by evaluating the zero-point energy of the quantum fluctuations that in our case reads $E_{ZP}(\theta, \ell) = \sum_{k\alpha} \epsilon_{k\alpha}(\theta, \ell)$, where θ and $\ell = K, K'$ specify the incommensurate order, and then finding its minimum as a function of the angle. In Fig. 6(a), we show the zero-point energy as a function of the polar angle θ for $P_z = -0.183$: the energy has six minima at $\pm\pi/6, \pm5\pi/6$ and $\pm\pi/2$. Since $E_{ZP}(\theta, \ell)$ does not depend on the second index for symmetry reasons, every minimum is doubly degenerate. In Fig. 6(b), a color plot shows how the zero-point energy is distributed on the same contours as the ones shown in Fig. 2. The Q -vector triplet minimizing the energy, given by $\theta = \pi/6$ and $\ell = K$, is plotted with white filled dots. Interestingly, Q_s^i and Q_s^b selected by quantum fluctuations lie, respectively, on the Γ - M and K - M directions. For convenience, we again show the flavor-wave spectrum as a function of the crystalline momentum for $P_z = -0.183$ in Fig. 6.

2. Dynamical structure factor

Let us define the following retarded Green's function:

$$G_{ab}(k, t) = -i\theta(t)\langle 0 | [\xi_{ka}(t), \xi_{-kb}] | 0 \rangle, \quad (\text{B12})$$

where we introduced the six-dimensional vector $\xi_k = (\mathbf{p}_k, \mathbf{x}_k)$. We can express $G_{ab}(k, t)$ in terms of the Green's function of the quasiparticles by means of a canonical trans-

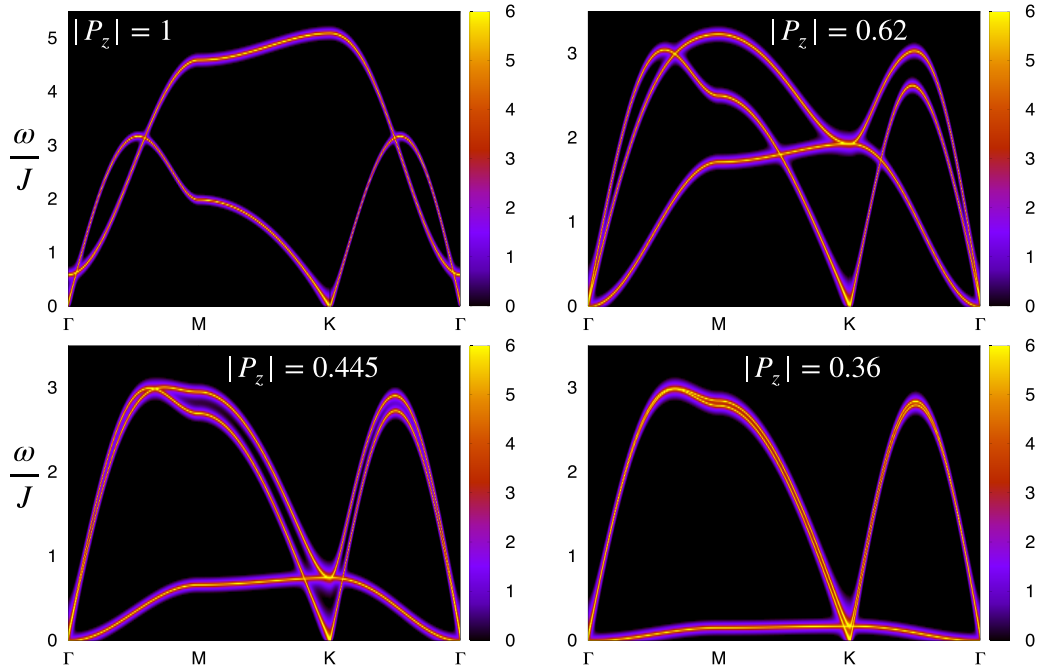


FIG. 7. Dynamic structure factor plotted in log scale for different polarization values $|P_z| = 1, 0.62, 0.445, 0.36$ for $J' = 0$. The ferromagnetic spin-wave mode that flattens to zero at $|P_z| = 1/3$ is well visible for all values of the layer imbalance.

formation that diagonalizes the Hamiltonian in Eq. (B9) and that preserves the canonical variables commutation relations. This is done via a transformation S_k so $S_k^\dagger \mathcal{J} S_k = \mathcal{J}$ and $S_k^\dagger \mathcal{H}_k S_k = \text{diag}(\epsilon_k, \epsilon_k)$, where \mathcal{H}_k is the 6×6 matrix appearing in Eq. (B9), and $\epsilon_k = (\epsilon_{k1}, \epsilon_{k2}, \epsilon_{k3})$. Such a transformation defines a set of new canonical coordinates, namely, $\xi_k = \tilde{\xi}_k S_k^\dagger$ and $\xi_{-k} = S_k \tilde{\xi}_{-k}$. In particular, let us define the following Hermitian matrix: $\tilde{\mathcal{J}}_k = i \mathcal{H}_k^{-1/2} \mathcal{J} \mathcal{H}_k^{-1/2}$, which can be rotated into the following diagonal form: $U_k^\dagger \tilde{\mathcal{J}}_k U_k = \text{diag}(\epsilon_k, -\epsilon_k)$. It is useful to introduce the following unitary transformation: $R_k = U_k T$, where $T = \exp(i\sigma^x \pi/4) \otimes \mathbb{I}_{3 \times 3}$. Finally, we can write the canonical transformation as the following: $S_k = \mathcal{H}_k^{-1/2} R_k D_k$, with $D_k = \text{diag}(\epsilon_k^{1/2}, \epsilon_k^{1/2})$.

Hence, Eq. (B12) can be rewritten in the following way:

$$G_{ab}(k, t) = \sum_{a'b'} [S_k^\dagger]_{a'a} [S_k]_{bb'} \tilde{G}_{a'b'}(k, t). \quad (\text{B13})$$

The Fourier transform of \tilde{G} , i.e., $\int_0^\infty \tilde{G}_{ab}(k, t) e^{i\omega t} dt$ is a 6×6 matrix with the following structure:

$$\tilde{G}(k, \omega) = \begin{pmatrix} \delta_{\alpha\beta} G_\alpha^X(k, \omega) & -\delta_{\alpha\beta} G_\alpha^{XP}(k, \omega) \\ \delta_{\alpha\beta} G_\alpha^{XP}(k, \omega) & \delta_{\alpha\beta} G_\alpha^X(k, \omega) \end{pmatrix}, \quad (\text{B14})$$

where $\alpha = \{1, 2, 3\}$ and the block diagonal terms are given by

$$G_\alpha^X(k, \omega) = \frac{1}{2} \left(\frac{1}{\omega - \epsilon_{k\alpha} + i\eta} - \frac{1}{\omega + \epsilon_{k\alpha} + i\eta} \right),$$

$$G_\alpha^{XP}(k, \omega) = \frac{i}{2} \left(\frac{1}{\omega - \epsilon_{k\alpha} + i\eta} + \frac{1}{\omega + \epsilon_{k\alpha} + i\eta} \right). \quad (\text{B15})$$

The Green's function evaluated along the imaginary Matsubara frequencies can be calculated starting from the one in Eq. (B15) via analytic continuation, i.e., by replacing $\omega + i\eta \rightarrow i\omega_n$, with $\omega_n = \frac{2\pi n}{\beta}$.

Since, flavor-flip processes where the majority flavor $|1\rangle$ flips into the minority ones ($|\alpha\rangle = |2\rangle, |3\rangle, |4\rangle$) are encoded by the operators S_α^1 , the dynamic structure factor can be written as

$$\begin{aligned} \mathcal{C}(k, \omega) &= -\text{Im} i \int_0^\infty dt e^{-i\omega t} \sum_\alpha \langle 0 | [S_\alpha^1(k, t), S_\alpha^1(-k)] | 0 \rangle \\ &= -\text{Im} i \int_0^\infty dt e^{-i\omega t} \sum_\alpha \langle 0 | ([x_{k\alpha}(t), x_{-k\alpha}] \\ &\quad + [p_{k\alpha}(t), p_{-k\alpha}] + i[p_{k\alpha}(t), x_{-k\alpha}] \\ &\quad - i[x_{k\alpha}(t), p_{-k\alpha}]) | 0 \rangle \\ &= -\text{Im} \text{Tr} [(\mathbb{I}_{6 \times 6} + \sigma^y \otimes \mathbb{I}_{3 \times 3}) G(k, \omega)]. \quad (\text{B16}) \end{aligned}$$

Let us note that, since the canonical transformation S_k is not unitary, the trace appearing in the last equation is affected nontrivially by the weights $[S_k]_{ab}$ in Eq. (B13). For this reason, it is useful to evaluate the dynamical structure factor which measures the absorption intensity. Figure 7 shows the dynamic structure factor for different values of the layer polarization and for $J' = 0$. We clearly recover the flavor-wave spectrum. In particular, we observe that the FM mode that flattens to zero at $|P_z| = 1/3$ is clearly visible for all values of the polarization. Therefore, the softening of this mode could be used as direct experimental evidence of the high degeneracy of the excitation spectrum which we identified as the main mechanism leading to the suppression of LRO and the onset of possible spin-liquid phases.

- [1] *Introduction to Frustrated Magnetism*, edited by C. Lacroix, P. Mendels, and F. Mila (Springer, Berlin, 2011).
- [2] L. Balents, Spin liquids in frustrated magnets, *Nature (London)* **464**, 199 (2010).
- [3] L. Savary and L. Balents, Quantum spin liquids: A review, *Rep. Prog. Phys.* **80**, 016502 (2017).
- [4] J. Knolle and R. Moessner, A field guide to spin liquids, *Annu. Rev. Condens. Matter Phys.* **10**, 451 (2019).
- [5] A. Kitaev, Anyons in an exactly solved model and beyond, *Ann. Phys.* **321**, 2 (2006).
- [6] N. Read and S. Sachdev, Large- N expansion for frustrated quantum antiferromagnets, *Phys. Rev. Lett.* **66**, 1773 (1991).
- [7] S. Sachdev and N. Read, Large N expansion for frustrated and doped quantum antiferromagnets, *Int. J. Mod. Phys. B* **05**, 219 (1991).
- [8] C. Castelnovo, R. Moessner, and S. L. Sondhi, Magnetic monopoles in spin ice, *Nature (London)* **451**, 42 (2008).
- [9] S. T. Bramwell and M. J. P. Gingras, Spin ice state in frustrated magnetic pyrochlore materials, *Science* **294**, 1495 (2001).
- [10] A. M. Tsvelik and P. Coleman, Order fractionalization in a Kitaev-Kondo model, *Phys. Rev. B* **106**, 125144 (2022).
- [11] C. Kuhlenkamp, W. Kadow, A. Imamoglu, and M. Knap, Tunable topological order of pseudo spins in semiconductor heterostructures, [arXiv:2209.05506](https://arxiv.org/abs/2209.05506).
- [12] A. Mishra, M. Ma, and F.-C. Zhang, Plaquette ordering in SU(4) antiferromagnets, *Phys. Rev. B* **65**, 214411 (2002).
- [13] C. Xu and C. Wu, Resonating plaquette phases in SU(4) Heisenberg antiferromagnet, *Phys. Rev. B* **77**, 134449 (2008).
- [14] R. K. Kaul, Quantum criticality in SU(3) and SU(4) antiferromagnets, *Phys. Rev. B* **84**, 054407 (2011).
- [15] M. Hermele and V. Gurarie, Topological liquids and valence cluster states in two-dimensional SU(N) magnets, *Phys. Rev. B* **84**, 174441 (2011).
- [16] M. Hermele, V. Gurarie, and A. M. Rey, Mott insulators of ultracold fermionic alkaline earth atoms: Underconstrained magnetism and chiral spin liquid, *Phys. Rev. Lett.* **103**, 135301 (2009).
- [17] M. G. Yamada, M. Oshikawa, and G. Jackeli, Emergent SU(4) symmetry in α -ZrCl₃ and crystalline spin-orbital liquids, *Phys. Rev. Lett.* **121**, 097201 (2018).
- [18] W. M. H. Natori, E. C. Andrade, and R. G. Pereira, SU(4)-symmetric spin-orbital liquids on the hyperhoneycomb lattice, *Phys. Rev. B* **98**, 195113 (2018).
- [19] D. Kiese, F. L. Buessen, C. Hickey, S. Trebst, and M. M. Scherer, Emergence and stability of spin-valley entangled quantum liquids in moiré heterostructures, *Phys. Rev. Res.* **2**, 013370 (2020).
- [20] X.-C. Wu, A. Keselman, C.-M. Jian, K. A. Pawlak, and C. Xu, Ferromagnetism and spin-valley liquid states in moiré correlated insulators, *Phys. Rev. B* **100**, 024421 (2019).
- [21] A. Keselman, L. Savary, and L. Balents, Dimer description of the SU(4) antiferromagnet on the triangular lattice, *SciPost Phys.* **8**, 076 (2020).
- [22] A. Keselman, B. Bauer, C. Xu, and C.-M. Jian, Emergent Fermi surface in a triangular-lattice SU(4) quantum antiferromagnet, *Phys. Rev. Lett.* **125**, 117202 (2020).
- [23] L. Savary, Quantum loop states in spin-orbital models on the honeycomb lattice, *Nat. Commun.* **12**, 3004 (2021).
- [24] A. V. Chubukov and T. Jolicoeur, Order-from-disorder phenomena in Heisenberg antiferromagnets on a triangular lattice, *Phys. Rev. B* **46**, 11137 (1992).
- [25] T. Jolicoeur, E. Dagotto, E. Gagliano, and S. Bacci, Ground-state properties of the $S = 1/2$ Heisenberg antiferromagnet on a triangular lattice, *Phys. Rev. B* **42**, 4800 (1990).
- [26] P. H. Y. Li, R. F. Bishop, and C. E. Campbell, Quasiclassical magnetic order and its loss in a spin- $\frac{1}{2}$ Heisenberg antiferromagnet on a triangular lattice with competing bonds, *Phys. Rev. B* **91**, 014426 (2015).
- [27] Z. Zhu and S. R. White, Spin liquid phase of the $s = \frac{1}{2}J_1 - J_2$ Heisenberg model on the triangular lattice, *Phys. Rev. B* **92**, 041105(R) (2015).
- [28] W.-J. Hu, S.-S. Gong, W. Zhu, and D. N. Sheng, Competing spin-liquid states in the spin- $\frac{1}{2}$ Heisenberg model on the triangular lattice, *Phys. Rev. B* **92**, 140403(R) (2015).
- [29] D.-V. Bauer and J. O. Fjærestad, Schwinger-boson mean-field study of the $J_1 - J_2$ Heisenberg quantum antiferromagnet on the triangular lattice, *Phys. Rev. B* **96**, 165141 (2017).
- [30] Y. Iqbal, W.-J. Hu, R. Thomale, D. Poilblanc, and F. Becca, Spin liquid nature in the Heisenberg $J_1 - J_2$ triangular antiferromagnet, *Phys. Rev. B* **93**, 144411 (2016).
- [31] R. Kaneko, S. Morita, and M. Imada, Gapless spin-liquid phase in an extended spin $1/2$ triangular Heisenberg model, *J. Phys. Soc. Jpn.* **83**, 093707 (2014).
- [32] S.-S. Gong, W. Zhu, J.-X. Zhu, D. N. Sheng, and K. Yang, Global phase diagram and quantum spin liquids in a spin- $\frac{1}{2}$ triangular antiferromagnet, *Phys. Rev. B* **96**, 075116 (2017).
- [33] S. N. Saadatmand and I. P. McCulloch, Symmetry fractionalization in the topological phase of the spin- $\frac{1}{2}J_1 - J_2$ triangular Heisenberg model, *Phys. Rev. B* **94**, 121111(R) (2016).
- [34] F. Ferrari and F. Becca, Dynamical structure factor of the $J_1 - J_2$ Heisenberg model on the triangular lattice: Magnons, spinons, and gauge fields, *Phys. Rev. X* **9**, 031026 (2019).
- [35] M. Drescher, L. Vanderstraeten, R. Moessner, and F. Pollmann, Dynamical signatures of symmetry broken and liquid phases in an $S = 1/2$ Heisenberg antiferromagnet on the triangular lattice, *Phys. Rev. B* **108**, L220401 (2023).
- [36] Z. Zhu, P. A. Maksimov, S. R. White, and A. L. Chernyshev, Topography of spin liquids on a triangular lattice, *Phys. Rev. Lett.* **120**, 207203 (2018).
- [37] A. Wietek, S. Capponi, and A. M. Läuchli, Quantum electrodynamics in 2+1 dimensions as the organizing principle of a triangular lattice antiferromagnet, [arXiv:2303.01585](https://arxiv.org/abs/2303.01585).
- [38] H. D. Scammell and M. S. Scheurer, Tunable superconductivity and möbius Fermi surfaces in an inversion-symmetric twisted van der Waals heterostructure, *Phys. Rev. Lett.* **130**, 066001 (2023).
- [39] H. D. Scammell and M. S. Scheurer, Displacement-field-tunable superconductivity in an inversion-symmetric twisted van der Waals heterostructure, *Phys. Rev. B* **109**, 035159 (2024).
- [40] Z. Sun, Y. Murakami, T. Kaneko, D. Golež, and A. J. Millis, Dynamical exciton condensates in biased electron-hole bilayers [arXiv:2312.06426](https://arxiv.org/abs/2312.06426).
- [41] A. V. Gorshkov, M. Hermele, V. Gurarie, C. Xu, P. S. Julienne, J. Ye, P. Zoller, E. Demler, M. D. Lukin, and A. M. Rey, Two-orbital SU(N) magnetism with ultracold alkaline-earth atoms, *Nat. Phys.* **6**, 289 (2010).

- [42] S. Taie, Y. Takasu, S. Sugawa, R. Yamazaki, T. Tsujimoto, R. Murakami, and Y. Takahashi, Realization of a $SU(2) \times SU(6)$ system of fermions in a cold atomic gas, *Phys. Rev. Lett.* **105**, 190401 (2010).
- [43] G. Pagano, M. Mancini, G. Cappellini, P. Lombardi, F. Schäfer, H. Hu, X.-J. Liu, J. Catani, C. Sias, M. Inguscio *et al.*, A one-dimensional liquid of fermions with tunable spin, *Nat. Phys.* **10**, 198 (2014).
- [44] M. A. Cazalilla and A. M. Rey, Ultracold Fermi gases with emergent $SU(N)$ symmetry, *Rep. Prog. Phys.* **77**, 124401 (2014).
- [45] L. Del Re and M. Capone, Selective insulators and anomalous responses in three-component fermionic gases with broken $SU(3)$ symmetry, *Phys. Rev. A* **98**, 063628 (2018).
- [46] D. Tusi, L. Franchi, L. Livi, K. Baumann, D. Benedicto Orenes, L. Del Re, R. Barfknecht, T.-W. Zhou, M. Inguscio, G. Cappellini, M. Capone, J. Catani, and L. Fallani, Flavour-selective localization in interacting lattice fermions, *Nat. Phys.* **18**, 1201 (2022).
- [47] E. Ibarra-García-Padilla, S. Dasgupta, H.-T. Wei, S. Taie, Y. Takahashi, R. T. Scalettar, and K. R. A. Hazzard, Universal thermodynamics of an $SU(n)$ Fermi-Hubbard model, *Phys. Rev. A* **104**, 043316 (2021).
- [48] S. Taie, E. Ibarra-García-Padilla, N. Nishizawa, Y. Takasu, Y. Kuno, H.-T. Wei, R. T. Scalettar, K. R. Hazzard, and Y. Takahashi, Observation of antiferromagnetic correlations in an ultracold $SU(N)$ Hubbard model, *Nat. Phys.* **18**, 1356 (2022).
- [49] M. Ferraretto, A. Richaud, L. Del Re, L. Fallani, and M. Capone, Enhancement of chiral edge currents in $(d+1)$ -dimensional atomic Mott-band hybrid insulators, *SciPost Phys.* **14**, 048 (2023).
- [50] D. Yamamoto and K. Morita, Engineering of a low-entropy quantum simulator for strongly correlated electrons using $SU(N)$ -symmetric cold atom mixtures, [arXiv:2311.08014](https://arxiv.org/abs/2311.08014).
- [51] F. Wu, T. Lovorn, E. Tutuc, and A. H. MacDonald, Hubbard model physics in transition metal dichalcogenide moiré bands, *Phys. Rev. Lett.* **121**, 026402 (2018).
- [52] Y. Zhang, N. F. Q. Yuan, and L. Fu, Moiré quantum chemistry: Charge transfer in transition metal dichalcogenide superlattices, *Phys. Rev. B* **102**, 201115(R) (2020).
- [53] H. Pan, F. Wu, and S. Das Sarma, Band topology, Hubbard model, Heisenberg model, and Dzyaloshinskii-Moriya interaction in twisted bilayer WSe_2 , *Phys. Rev. Res.* **2**, 033087 (2020).
- [54] M. H. Naik and M. Jain, Ultraflatbands and shear solitons in moiré patterns of twisted bilayer transition metal dichalcogenides, *Phys. Rev. Lett.* **121**, 266401 (2018).
- [55] E. C. Regan, D. Wang, C. Jin, M. I. Bakti Utama, B. Gao, X. Wei, S. Zhao, W. Zhao, Z. Zhang, K. Yumigeta, M. Blei, J. D. Carlström, K. Watanabe, T. Taniguchi, S. Tongay, M. Crommie, A. Zettl, and F. Wang, Mott and generalized Wigner crystal states in WSe_2/WS_2 moiré superlattices, *Nature (London)* **579**, 359 (2020).
- [56] Y. Tang, L. Li, T. Li, Y. Xu, S. Liu, K. Barmak, K. Watanabe, T. Taniguchi, A. H. MacDonald, J. Shan, and K. F. Mak, Simulation of Hubbard model physics in WSe_2/WS_2 moiré superlattices, *Nature (London)* **579**, 353 (2020).
- [57] C. Jin, Z. Tao, T. Li, Y. Xu, Y. Tang, J. Zhu, S. Liu, K. Watanabe, T. Taniguchi, J. C. Hone, L. Fu, J. Shan, and K. F. Mak, Stripe phases in WSe_2/WS_2 moiré superlattices, *Nat. Mater.* **20**, 940 (2021).
- [58] Y. Shimazaki, I. Schwartz, K. Watanabe, T. Taniguchi, M. Kroner, and A. Imamoğlu, Strongly correlated electrons and hybrid excitons in a moiré heterostructure, *Nature (London)* **580**, 472 (2020).
- [59] L. Wang, E.-M. Shih, A. Ghiotto, L. Xian, D. A. Rhodes, C. Tan, M. Claassen, D. M. Kennes, Y. Bai, B. Kim, K. Watanabe, T. Taniguchi, X. Zhu, J. Hone, A. Rubio, A. N. Pasupathy, and C. R. Dean, Correlated electronic phases in twisted bilayer transition metal dichalcogenides, *Nat. Mater.* **19**, 861 (2020).
- [60] Y. Xu, S. Liu, D. A. Rhodes, K. Watanabe, T. Taniguchi, J. Hone, V. Elser, K. F. Mak, and J. Shan, Correlated insulating states at fractional fillings of moiré superlattices, *Nature (London)* **587**, 214 (2020).
- [61] X.-P. Yao, Y. Gao, and G. Chen, Topological chiral spin liquids and competing states in triangular lattice $SU(n)$ mott insulators, *Phys. Rev. Res.* **3**, 023138 (2021).
- [62] X. Huang, T. Wang, S. Miao, C. Wang, Z. Li, Z. Lian, T. Taniguchi, K. Watanabe, S. Okamoto, D. Xiao, S.-F. Shi, and Y.-T. Cui, Correlated insulating states at fractional fillings of the $WS_2/$ moiré lattice, *Nat. Phys.* **17**, 715 (2021).
- [63] D. M. Kennes, M. Claassen, L. Xian, A. Georges, A. J. Millis, J. Hone, C. R. Dean, D. Basov, A. N. Pasupathy, and A. Rubio, Moiré heterostructures as a condensed-matter quantum simulator, *Nat. Phys.* **17**, 155 (2021).
- [64] J. Zang, J. Wang, J. Cano, A. Georges, and A. J. Millis, Dynamical mean-field theory of moiré bilayer transition metal dichalcogenides: Phase diagram, resistivity, and quantum criticality, *Phys. Rev. X* **12**, 021064 (2022).
- [65] Y. Zeng, N. Wei, and A. H. MacDonald, Layer pseudospin magnetism in a transition metal dichalcogenide double-moiré system, *Phys. Rev. B* **106**, 165105 (2022).
- [66] P. Tscheppe, J. Zang, M. Klett, S. Karakuzu, A. Celarier, Z. Cheng, C. A. Marianetti, T. A. Maier, M. Ferrero, A. J. Millis, and T. Schäfer, Magnetism and metallicity in moiré transition metal dichalcogenides, *Proc. Nat. Acad. Sci. USA* **121**, e2311486121 (2024).
- [67] J. Motruk, D. Rossi, D. A. Abanin, and L. Rademaker, Kagome chiral spin liquid in transition metal dichalcogenide moiré bilayers, *Phys. Rev. Res.* **5**, L022049 (2023).
- [68] D. Rossi, J. Motruk, L. Rademaker, and D. A. Abanin, Schwinger boson study of the $J_1-J_2-J_3$ kagome Heisenberg antiferromagnet with Dzyaloshinskii-Moriya interactions, *Phys. Rev. B* **108**, 144406 (2023).
- [69] Y.-H. Zhang, D. N. Sheng, and A. Vishwanath, $SU(4)$ chiral spin liquid, exciton supersolid, and electric detection in moiré bilayers, *Phys. Rev. Lett.* **127**, 247701 (2021).
- [70] Y. Xu, K. Kang, K. Watanabe, T. Taniguchi, K. F. Mak, and J. Shan, A tunable bilayer Hubbard model in twisted WSe_2 , *Nat. Nanotechnol.* **17**, 934 (2022).
- [71] Z. Zhang, E. C. Regan, D. Wang, W. Zhao, S. Wang, M. Sayyad, K. Yumigeta, K. Watanabe, T. Taniguchi, S. Tongay, M. Crommie, A. Zettl, M. P. Zaletel, and F. Wang, Correlated interlayer exciton insulator in heterostructures of monolayer WSe_2 and moiré WS_2/WS_2 , *Nat. Phys.* **18**, 1214 (2022).
- [72] K. Penc, M. Mambrini, P. Fazekas, and F. Mila, Quantum phase transition in the $SU(4)$ spin-orbital model on the triangular lattice, *Phys. Rev. B* **68**, 012408 (2003).
- [73] C. Schrade and L. Fu, Spin-valley density wave in moiré materials, *Phys. Rev. B* **100**, 035413 (2019).

- [74] C. Zhang, H.-K. Jin, and Y. Zhou, Variational Monte Carlo approach to the SU(4) spin-orbital model on the triangular lattice, *Phys. Rev. B* **109**, 125103 (2024).
- [75] K. I. Kugel and D. I. Khomskii, The Jahn-Teller effect and magnetism: Transition metal compounds, *Sov. Phys. Usp.* **25**, 231 (1982).
- [76] A. Joshi, M. Ma, F. Mila, D. N. Shi, and F. C. Zhang, Elementary excitations in magnetically ordered systems with orbital degeneracy, *Phys. Rev. B* **60**, 6584 (1999).
- [77] We note that, differently from the states sketched in Fig. 1 for $|P_z| < 1/3$, these degenerate states yield homogeneous polarisation.
- [78] A. L. Chernyshev and M. E. Zhitomirsky, Spin waves in a triangular lattice antiferromagnet: Decays, spectrum renormalization, and singularities, *Phys. Rev. B* **79**, 144416 (2009).
- [79] L. Del Re, M. Fabrizio, and E. Tosatti, Nonequilibrium and non-homogeneous phenomena around a first-order quantum phase transition, *Phys. Rev. B* **93**, 125131 (2016).
- [80] T. Jolicoeur and J. C. Le Guillou, Spin-wave results for the triangular Heisenberg antiferromagnet, *Phys. Rev. B* **40**, 2727 (1989).
- [81] J. Villain, R. Bidaux, J.-P. Carton, and R. Conte, Order as an effect of disorder, *J. Phys.* **41**, 1263 (1980).
- [82] M. E. Zhitomirsky, M. V. Gvozdkova, P. C. W. Holdsworth, and R. Moessner, Quantum order by disorder and accidental soft mode in $\text{Er}_2\text{Ti}_2\text{O}_7$, *Phys. Rev. Lett.* **109**, 077204 (2012).
- [83] T. A. Tóth, A. M. Läuchli, F. Mila, and K. Penc, Three-sublattice ordering of the SU(3) Heisenberg model of three-flavor fermions on the square and cubic lattices, *Phys. Rev. Lett.* **105**, 265301 (2010).
- [84] B. Bauer, P. Corboz, A. M. Läuchli, L. Messio, K. Penc, M. Troyer, and F. Mila, Three-sublattice order in the SU(3) Heisenberg model on the square and triangular lattice, *Phys. Rev. B* **85**, 125116 (2012).
- [85] G. Jackeli and A. Avella, Quantum order by disorder in the Kitaev model on a triangular lattice, *Phys. Rev. B* **92**, 184416 (2015).
- [86] This is not the only possible choice to define the strong fluctuations region in the phase diagram. Sometimes $n_1 = 0$ is chosen to mark the onset of possible spin-liquid phases. However, we found that our choice is applicable to the SU(2)-limit without any ambiguity. In fact, for spin 1/2, $n_1 = 0$ would yield a negative expectation value of the order parameter instead of zero, and therefore such a choice would underestimate the role of quantum fluctuations.
- [87] P. W. Anderson, An approximate quantum theory of the antiferromagnetic ground state, *Phys. Rev.* **86**, 694 (1952).
- [88] B. Bernu, P. Lecheminant, C. Lhuillier, and L. Pierre, Exact spectra, spin susceptibilities, and order parameter of the quantum Heisenberg antiferromagnet on the triangular lattice, *Phys. Rev. B* **50**, 10048 (1994).
- [89] A. J. Beekman, L. Rademaker, and J. van Wezel, An introduction to spontaneous symmetry breaking, *SciPost Phys. Lect. Notes*, **11** (2019).
- [90] T. Botzung and P. Nataf, Exact diagonalization of SU(N) Fermi-Hubbard models, [arXiv:2309.09965](https://arxiv.org/abs/2309.09965).
- [91] Y. Miyazaki, G. Marmorini, N. Furukawa, and D. Yamamoto, Linear flavor-wave analysis of SU(4)-symmetric tetramer model with population imbalance, *J. Phys. Soc. Jpn.* **91**, 073702 (2022).
- [92] Arvind, B. Dutta, N. Mukunda, and R. Simon, The real symplectic groups in quantum mechanics and optics, *Pramana* **45**, 471 (1995).